CHEMISTRY OF MATERIALS

pubs.acs.org/cm

Article

Fast Charging from Low Li-Ion Migration Barriers in Wadsley−Roth $NaNb_7O_{18}$ Anodes

Arava Zohar, Tianyu Li, Yucheng Zhou, Kira E. Wyckoff, Alexander Justice Bologna, Ashlea Patterson, Laurent Pilon, and Ram Seshadri*

Cite This: https://doi.org/10.1021/acs.chemmater.4c02980

Read Online

ACCESS | Metrics & More | Article Recommendations | Supporting Information

ABSTRACT: While current electric vehicles are approaching internal combustion engine vehicles in terms of driving range, the relatively long charging time of batteries represents a fundamental challenge. Materials used as anodes show slow ion insertion, which is usually responsible for the inability of automotive batteries to charge rapidly. To address this challenge, research into the kinetics of solid-state ion insertion is needed. The essential properties of fast-charging electrodes include high electronic and ionic conductivities, mechanical and chemical stability, and a 3D framework with channels for ion transport, especially when the added cost of nanostructuring is not desirable. In recent years, there has been increasing recognition that Nb-based shear-structured oxides, many belonging to the Wadsley−Roth class of compounds, show fast insertion. We focus here on $NaNb_7O_{18}$, a member of this Wadsley−Roth family that has not been previously studied as an anode material for Li-ion batteries. Bulk $NaNb_7O_{18}$ is shown to demonstrate high cyclability, retaining over 90% capacity even after 1000 cycles at a relatively rapid 2C rate. Potentiometric entropy measurements support the presence of two-phase reaction mechanisms (which is usually contraindicated for fast charging) and point to the role of intralayer ion ordering. The energy barrier between Li sites is found to be low, which is likely to be an important contributor to the fast lithiation kinetics in this compound. The electrochemical analysis points to apparent diffusion coefficients in the range of 10^{-12} cm^2 s^{-1} and a low overpotential close to 130 mV. An analysis of the lithiation kinetics of related Wadsley−Roth compounds finds that fast intercalation/deintercalation is robust across this family of compounds, regardless of the details of the intercalation mechanism.

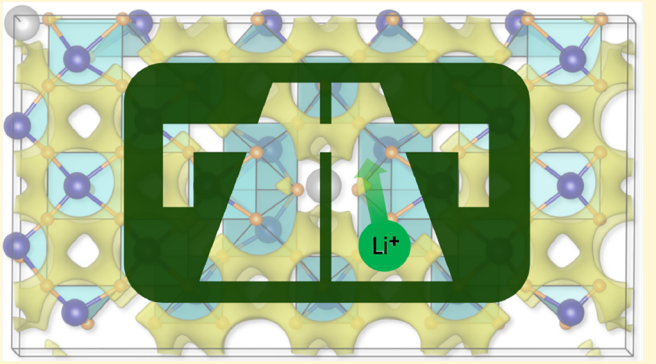

INTRODUCTION

Excess CO_2 emissions are one of the primary causes of climate change, and it is widely agreed that electrification of transportation can help reduce these emissions by using rechargeable batteries and electric motors in fuel and power vehicles rather than hydrocarbon fuels and combustion engines. While rechargeable Li-ion batteries in automobiles have improved their capacities sufficiently so that range is no longer a pressing issue, relatively slow battery charging rates are still an issue. The US Department of Energy has stated the aim of improving battery performance in electric vehicles to achieve a charging experience similar to refueling, which typically takes a few minutes. A battery with fast-charging capability requires a negative electrode (anode) that can intercalate ions rapidly. Over the years, many efforts have focused on increasing the capacity of cathode materials in Li-ion batteries.[1−3] However, the anode material, graphite, remained largely unchanged. Graphite is widely used as an anode due to its high theoretical Li-ion storage capacity of 372 mAh g^{-1},[4] reversible insertion, and abundance. However, its main drawback is a relatively slow charging rate, and increasing the charging rate of graphite electrodes beyond certain low thresholds can cause safety issues. The low voltage for Li-ion insertion in graphite also results in electrolyte decomposition and the formation of a solid electrolyte interphase (SEI), slowing down kinetics and reducing efficiency.[5−7] New materials capable of fast-charging rates are necessary to bridge the gap between current battery performance and future goals.

New electrode materials for efficient and fast electrochemical energy storage should feature several properties, including high electronic and ionic conductivities, mechanical and chemical stability, suitable redox voltage, and channels in the structure that enable ion insertion. The selected elemental electrode materials should also ideally be nontoxic, accessible, abundant, and possess high specific capacity. Oxides of transition metals,

Received: October 29, 2024
Revised: January 23, 2025
Accepted: January 24, 2025

such as Ti, V, Nb, and Mo, can meet these requirements. These oxides display various crystal structures (e.g., rutile, spinel, layered, and so on), which opens exciting opportunities for discovering materials with high ion diffusivity in electrodes. These elements have redox potentials between 1.0 and 2.0 V vs Li^+/Li, alleviating concerns about safety and stability in this voltage range, as SEI formation and Li dendrite growth are associated with potentials below 1.0 V.

Niobium oxide compounds with crystallographic shear structures, including the Wadsley−Roth compounds, have demonstrated impressive capacity performance and retention at high rates.[8−11] Their capacity can be explained by the multiple stable oxidation states of niobium, allowing for storage of more than one electron per transition metal. These multiple oxidation states originate from partially filled d-orbitals, leading to distinctive characteristics, such as insulator-to-metal transitions[12] and second-order Jahn−Teller distortions.[13] Both phenomena result from electron occupation that modifies the structure. During cell cycling, these changes can affect the charging rate performance. For example, the second-order Jahn−Teller distortion leads to displacement of the metal in the center of the octahedral, potentially creating more space for Li ions and elevating the diffusion coefficient compared to nondistorted octahedra.[14] This understanding can explain why TiO_2 cannot be fully lithiated using electrochemical methods.[15] In addition to acceptable capacity performance, the charging rates of shear-structured niobium oxide structures have been impressive, exceeding 100 mAh g^{-1} within 6 min of charging.[12,16−18] These compounds possess corner-shared polyhedra that form open channels for Li ions and edge-shared polyhedra that keep the structure stable during cycling.

Ion insertion is usually expected to evolve through two main mechanisms: two-phase reactions and solid-solution reactions. A two-phase reaction involves the coexistence of the starting compound with a new phase. This reaction should have a well-defined border between the two phases. In a solid-solution reaction, the mobile ion mixes in the existing phase until a new phase forms. A first-principles thermodynamics study has found that a high degree of Li ordering between different sites in the host crystal is associated with two-phase reactions and slow kinetics.[19,20] Conversely, a low degree of Li ordering between different sites in the host crystal lowers the migration barrier and is often associated with solid-solution behavior and faster kinetics. Low entropy of Li insertion creates a barrier for more Li ions to intercalate into subsequent sites.[21] Therefore, an approach to achieve faster kinetics is to reduce Li ordering by allowing more solid-solution reactions. This approach aligns with that of Clément et al.[22] and shows improved performance and rates when mixing multiple cations in disordered rock-salt cathodes. Cation disorder can thus reduce the degree of Li ordering and allow for faster kinetics. For clarity, the term "order" is mentioned from two different perspectives: the ordering of the intercalated Li ion in the host crystal, as opposed to the ordering of cations in the host, notably in crystals in which different metal cations occupy the same crystallographic sites.

In this study, we present a member of the Wadsley−Roth family, $NaNb_7O_{18}$, investigated for the first time as an anode for Li-ion batteries. This composition was introduced in 1984 by Marinder and Sundberg, and the structure was determined by using high-resolution electron microscopy and multislice calculations of simulated images.[23] There are two possible types of sites for Li-ion insertion. Thanks to the high degree of cation order in this compound and the limited number of insertion sites, it can be used as a case study to examine whether the nature of the insertion affects the kinetics. We find that $NaNb_7O_{18}$ is an electrode material with impressive capacities at high rates despite displaying two-phase behavior.

To obtain a broader understanding of how the Wadsley−Roth family hosts Li insertion, we have examined five different compounds using the galvanostatic intermittent titration technique (GITT)[24,25] and extracted diffusion coefficients and overpotentials. The results show a relatively tight range of diffusion coefficients and overpotentials across the different compounds, with no particular dependence on the precise nature of Li insertion, whether through solid-solution or two-phase reactions.

MATERIALS AND METHODS

Preparation of $NaNb_7O_{18}$. $NaNb_7O_{18}$ powders were prepared from stoichiometric amounts of $NaNbO_3$ (Aldrich Chemical Co., 99%) and Nb_2O_5 (Materion, 99.95%). The starting materials were ground in an agate mortar for 10 min, pressed into 350 mg pellets under 4.0 tons in a 10 mm diameter die, and placed into a 10 cm^3 alumina crucible, which was heated at 800 °C for 24 h and then at 1150 °C for 48 h. The sample was slowly cooled to room temperature in the furnace. The preparation of other samples employed in this study is described in the Supporting Information.

Powder Diffraction and Rietveld Refinements. Powder X-ray diffraction (PXRD) measurements were performed by using a PANalytical Empyrean powder diffractometer in reflection mode with a Cu Kα radiation source. Rietveld analysis was performed to confirm the structure and phase purity using the TOPAS[26] software package. Crystal structures were visualized using VESTA.[27] High-resolution synchrotron powder X-ray diffraction (SXPD) data were collected at beamline 2-1 at the Stanford Synchrotron Radiation Source using a wavelength of λ = 0.1173 Å. A 2D PerkinElmer a-Si flat panel detector was used to collect the data.

Operando X-ray Diffraction under Electrochemical Cycling. Operando X-ray diffraction data were collected during electrochemical cycling using an in-house cell with a Be window. The cell was placed in a PANalytical Empyrean powder diffractometer in reflection mode with a Cu−Kα radiation source.

Raman Spectroscopy. Raman spectroscopy was performed at room temperature using a Horiba Jobin Yvon T64000 open-frame confocal microscope, operating with an excitation laser wavelength of λ = 488 nm, a monochromator, and an LN_2-cooled CCD array detector. Filters were used to reduce the laser to 50% of its original intensity to prevent beam damage to the samples. Spectra were calibrated by referencing the spectrum of monocrystalline silicon, which has a peak at 521 cm^{-1}.

Scanning Electron Microscopy. Scanning electron microscopy (SEM) images of powder samples placed on double-sided carbon tape were acquired on an Apreo C FEG (ThermoFisher) microscope using secondary electrons and InLens detectors with a 10 keV accelerating voltage and a 0.8 nA current.

Electrochemistry. The synthesized $NaNb_7O_{18}$ was mixed with the binder and carbon in an 8:1:1 ratio. *N*-methyl-2-pyrrolidone solvent was added to the mixture to form a thick slurry, which was cast on Cu foil. After drying in a vacuum furnace, 10 mm electrodes were punched and assembled into coin cells. The conductive carbon employed was TIMCAL SuperP, and the binder was polyvinylidene fluoride (Kynar 2800). The cast foils were punched into 10 mm disk electrodes. The typical loading of active materials on the electrodes was between 3 and 4 mg cm^{-2}. Coin cells (MTI parts, 2032 SS casings) were assembled from the electrodes in an argon-filled glovebox using polished Li foil (Sigma-Aldrich) as the counter electrode, 16 mm glass fiber separators (Whatman GF/D), and a 1 M $LiPF_6$ EC/DMC electrolyte (Sigma-Aldrich). Cells were crimped under 8 tons of pressure. Electrochemistry experiments were performed on the assembled coin cells using a BioLogic potentiostat

https://doi.org/10.1021/acs.chemmater.4c02980
Chem. Mater. XXXX, XXX, XXX−XXX

VMP 3 (EC-Lab v11.43) at 25 °C in a controlled environment. To test extended cycling performance, galvanostatic cycling was performed at a cycling rate of 2C between 1 and 3 V for 200 cycles with a 5 min rest interval between cycles. For variable rate cycling, cycling rates of C/10, C/5, 1C, 2C, 5C, and 10C were used, each for 5 cycles. C rates were calculated based on one Li per transition metal and a theoretical capacity of 195.1 mAh g^{-1}.

Inductively Coupled Plasma Optical Emission Spectroscopy. To better understand the stability of the $NaNb_7O_{18}$ structure, the Na/Nb ratio was characterized by inductively coupled plasma-optical emission spectroscopy (ICP-OES Agilent 5800). Three samples were created from cathode casts: a "pristine" sample that was only cast, a "rested" sample that was assembled into a coin cell but never cycled, and a "cycled" sample that was assembled into a coin cell and cycled. To prepare samples, the active material (≈8 mg) was scrapped from the copper current collector and washed 3 times in 5 cm^3 acetone to remove the PVDF binder. Samples were digested in 1 cm^3 HF/HNO_3 (50:50 by volume, Fisher Scientific, Trace Metals grade). Conductive carbon was removed from the digestions through centrifugal action after dilution. Certified Na and Nb standards (Inorganic Ventures) were used to create a calibration curve with relative standard error values below 3% and correlation coefficients above 0.99999. Relative standard deviation values for all samples fell below 1.

Potentiometric Entropy Measurements. The potentiometric entropy measurement technique was performed on coin cells with $NaNb_7O_{18}$ working electrodes and Li metal counter electrodes, using the setup described previously.[21,28,29] Specifically, the open-circuit voltage $U_{OCV}(x,T)$ and entropic potential $\partial U_{OCV}(x,T)/\partial T$ of coin cells were measured as functions of Li composition x. Over the measurements at 20 °C, a series of 30 min constant current pulses corresponding to C/10 were imposed, each followed by a relaxation period (270 min). During the relaxation periods, a step-like temperature profile was applied to the coin cell from 15 to 25 °C in 5 °C increments with a thermoelectric cold plate (TE technology, CP-121). Simultaneously, the corresponding coin cell potential evolution was recorded with a potentiostat (BioLogic, model VSP-300). Near the end of every temperature step, it was verified that the coin cell had reached thermodynamic equilibrium if (i) the temperature difference between the cold plate and the top of the coin cell was less than 0.1 °C and (ii) the time rate of change of the open-circuit voltage $\partial U_{OCV}(x,T)/\partial t$ was less than 1 mV h^{-1}.

RESULTS AND DISCUSSION

$NaNb_7O_{18}$ powders were prepared from ceramic synthesis and characterized by SXPD and Raman spectroscopy, as presented in Figure 1. Rietveld refinement of using the TOPAS suite of programs[26] shows a single-phase fit to the reported *Immm* structure, with structural details presented in the Supporting Information section. The phase diagram of Na_2O and Nb_2O_5 suggests that other stable compositions could result from this synthesis.[30] We therefore employed Raman spectroscopy as a complementary method to X-ray diffraction. Figure 1b shows Raman peaks at 131.0, 147.8, 199.7, 219.9, 263.9, 307.6, 343.7, 446.6, 553.78, 618.4, 650.14, 847.3, 886.74, and 990.9 cm^{-1}. We can establish that the spectrum is consistent with the refined structure and composition on the basis of prior studies on a series of niobium oxide reference compounds.[31−35] The low-frequency peaks (last three) represent different Nb−O longitudinal vibration modes, where 990 cm^{-1} is associated with corner-sharing oxygen and the other two (847.3, 886.74 cm^{-1}) are associated with two different environments of the edge-sharing Nb−O bonds. Peaks in the 600−660 cm^{-1} range are related to Nb−O transverse vibrational modes. The 550 cm^{-1} peak is associated with the block structure. The higher frequency (210−350 cm^{-1}) peaks are associated with asymmetric octahedra resulting from disorder, and therefore, these peaks are broad. The peaks below 200 cm^{-1} are assigned to metal−metal bonds. Both X-ray diffraction and Raman spectroscopy show a good fit with the literature, indicating that we synthesized a pure compound. SEM on the bulk powder particles is shown as an inset and reveals highly crystalline particles about 1 to 5 μm in size.

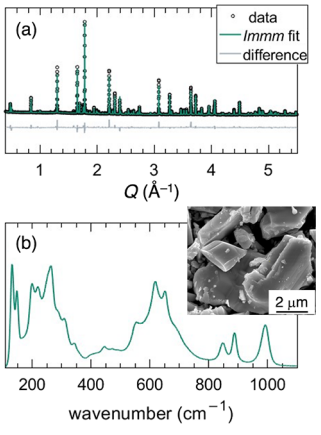

Figure 1. (a) Rietveld refinement of powder X-ray diffraction data and (b) Raman spectrum collected on $NaNb_7O_{18}$ powder. The inset displays an SEM image of an as-prepared powder.

Figure 2a shows projections of the structure of $NaNb_7O_{18}$. This structure has 4 × 4 ReO_3 blocks tiled in a zigzag pattern with crystallographic shear at the edges. Each unit cell contains sodium located at the edges of blocks in channels that are not accessible to Li ions. Figure 2b shows the diffusion landscape of Li ions calculated using the bond valence sum (BVS) method[36] using the SoftBV code.[37,38] The isosurface was set to $\delta\nu$ = 0.1, where $\delta\nu$ is indicative of the half-width (in valence units) of the volume accessible to the mobile ion. The connected isosurface indicates low energy barriers for intra-block hopping in the $a-b$ plane and also low energy pathways along the c axis within the blocks. A value of $\delta\nu$ = 0.1 is highly

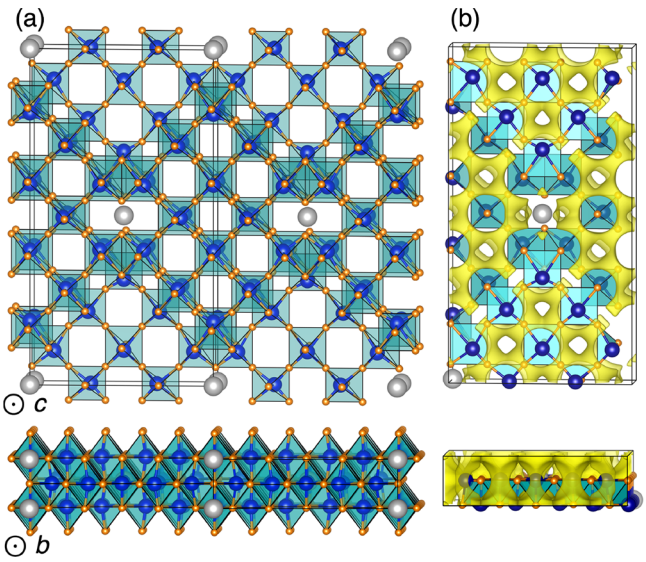

Figure 2. (a) Projections of the crystal structure of $NaNb_7O_{18}$ and (b) Li^+ valence bond map for an isosurface with $\Delta\nu$ = 0.1 valence units created by using softBV, showing connected pathways for high Li^+ diffusion in all directions of the crystal structure.

https://doi.org/10.1021/acs.chemmater.4c02980
Chem. Mater. XXXX, XXX, XXX−XXX

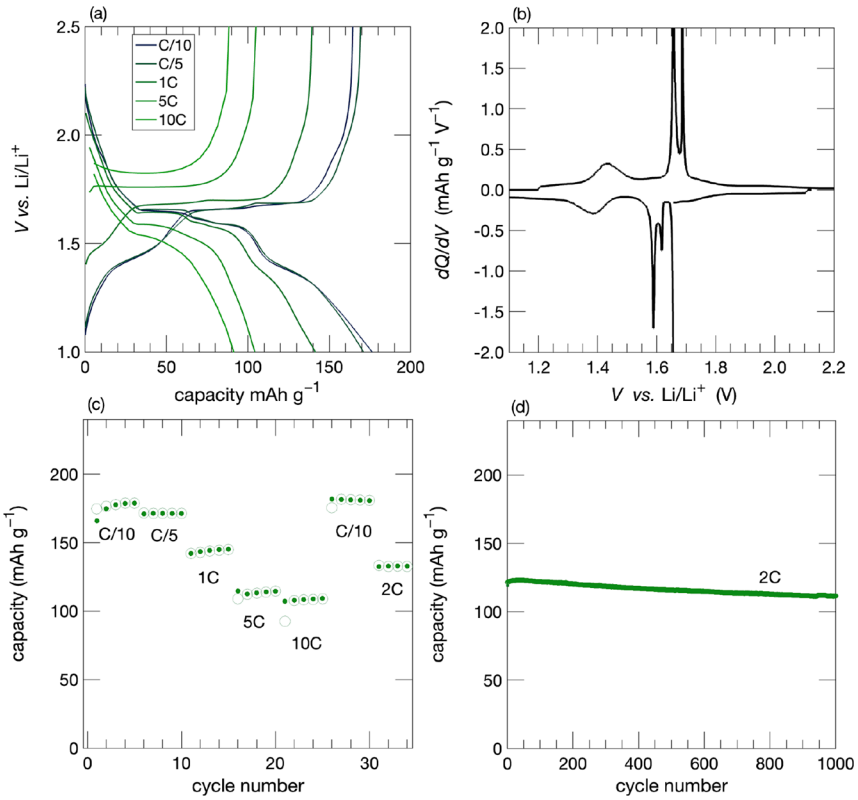

Figure 3. (a) Charging and discharging profile of the $NaNb_7O_{18}$ anode vs Li metal at C/10, C/5, 1C, 5C, and 10C rates between 1 and 3.0 V (where 1C = 0.195 A g^{-1}). (b) dQ/dV as a function of the voltage of the first cycle at the C/10 rate. (c) Variable rate galvanostatic cycling rates from C/10 to 10C. Open circles represent charging capacity, and the closed circles represent discharging capacity. (d) Long-term galvanostatic with good capacity retention at 2C (≥90%).

suggestive of low migration barriers and usually corresponds to a barrier height of less than 200 meV. These multiple channels for Li-ion transport are continuous pathways and consistent with similar Wadsley−Roth Li-ion transport. A similar analysis for Na ions within this compound suggests that Na ions can occupy the channels but cannot hop along the *c* axis (down channels) or within the *a*−*b* plane due to high migration barriers.

The electrochemical performance of $NaNb_7O_{18}$ was tested in a half-cell configuration vs Li metal and is presented in the four panels of Figure 3. Panel (a) shows the charging and discharging profiles of different galvanostatic cycling rates. At low rates, the compound can store 175 mAh g^{-1}. The observed value is slightly lower than the theoretical one-electron capacity per Nb, which is 195 mAh g^{-1}, perhaps due to the large particle size and due to Li transport bottlenecks near the Na sites in the structure, as seen in Figure 2. Smaller particles that could be prepared by ball milling or by soft chemical synthesis can be considered as a means for demonstrating higher capacities in this compound, as seen in other studies of Wadsley−Roth electrodes.[39−41] Panel (b) shows the derivative of the charge as a function of the voltage, dQ/dV. This highlights the Nb redox peaks along the reaction path. There are two intense peaks between 1.65 and 1.55 V and another smaller peak at 1.4 V. The capacity associated with these sharp peaks is the representation of phase transition around the redox voltage of the niobium during each lithiation and delithiation. It provides evidence that a large fraction of the reaction is a two-phase reaction when a slow galvanostatic cycle is applied because the sharp peak results from a constant voltage as long as the two phases coexist. For a higher cycling rate, the two-phase reaction (plateau in the *I*−*V* curve) is smaller, though a substantial capacity is still stored at those rates.

To verify that Na in the electrodes is not exchanged with Li or otherwise contributing to the electrochemistry, we have carried out inductively coupled plasma atomic emission spectrometry (ICP-AES) spectroscopy with standards for pristine $NaNb_7O_{18}$, $NaNb_7O_{18}$ after resting in cells for 24 h, and after 2 weeks of cycling at a 2C rate, with the electrode dissolved in aqua regia and diluted appropriately. The expected elemental ratio of Na/Nb is 1:7 or 0.143. The as-prepared sample was measured to have a Na/Nb ratio of 0.141. The samples that were rested in cells and cycled, respectively, measured 0.171 and 0.167, suggesting no Na loss. This supports the bond valence analysis, suggesting that Na in the structure is not mobile.

The capacity measurements of $NaNb_7O_{18}$ at high rates and long-term cycling at 2C (30 min for charging or discharging) were performed, as illustrated in Figure 3c,d, and can bring insight regarding the Li-ion kinetics in two-phase reactions. At high rates, the $NaNb_7O_{18}$ half-cell can charge up to 95 mAh g^{-1} in 6 min. This is despite the relatively large particle sizes noted, on the order of 1−5 μm. The long-term cycling of the half cell at 2C shows that 90% of its original capacity is retained after 1000 cycles (111 mAh g^{-1} versus initial capacity of 121 mAh g^{-1}). The capacity retention hints that the material does not have significant structural change or decomposition during those reactions. Two reasons can explain these remarkable results: (i) the electrochemical reaction voltage

https://doi.org/10.1021/acs.chemmater.4c02980
Chem. Mater. XXXX, XXX, XXX−XXX

window does not involve the decomposition of any of the compounds in the cell, including the electrolyte and the additives, and hence, prevents SEI formation on this anode and (ii) the Wadsley−Roth material contains open Li-ion channels and a shear structure that forms a stable framework even when a large number of ions leaves the structure and ensures long-term cyclability.

The structural evolution during Li insertion was observed by operando X-ray diffraction using a custom cell with a Be window. Figure 4 shows the first charge and discharge cycles at

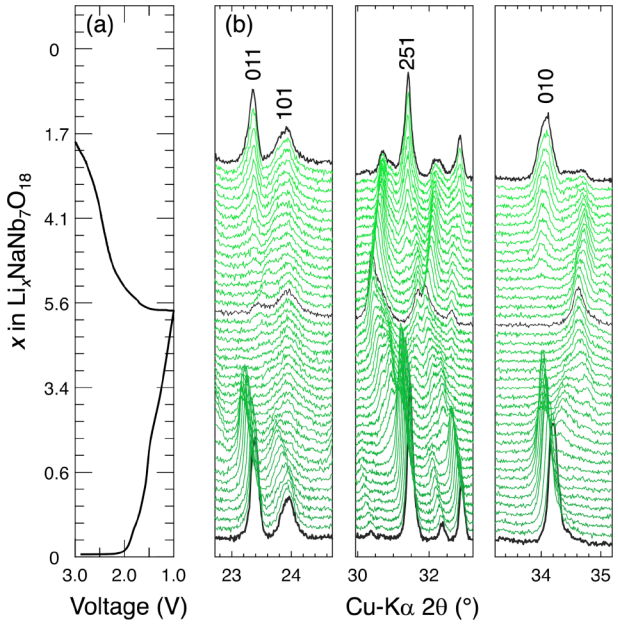

Figure 4. Operando XRD of $NaNb_7O_{18}$ discharged to 1.0 V and charged to 3.0 V at a C/10 rate. (a) Electrochemical data and (b) three panels display select diffraction peaks.

a C/10 rate. Panel (a) presents galvanostatic measurements as a function of x in $Li_xNaNb_7O_{18}$. The three right panels (b) show the diffraction patterns for selected peaks (the complete data is available in the SI), starting with the pristine electrode at the bottom and stacking up along the electrochemical reaction, recorded in panel (a). The pristine $NaNb_7O_{18}$ X-ray diffraction displayed a pure phase, and the peaks gradually migrated to lower angles as Li ions were inserted into the structure during the charging step. Much of the volume expansion seems associated with an expansion in the b cell parameter, which corresponds to the long direction of the channels that contain Na^+. After the first plateau at about 1.6 V, the diffraction intensity decreases, and a new phase starts appearing. When a phase transition occurs, the symmetry of the structure appears to remain the same with a contraction of the a−b plane and expansion along c. Lattice contraction in the block unit and layer expansion along c are commonly observed in other Wadsley−Roth compounds during Li intercalation[42] due to metal−metal bond formation along the edges of the blocks in these structures. The expansion along c potentially accommodates an additional Li-ion volume.

During discharge, a recovery of the original phase position can be observed, as it slowly forms and shows a peak intensity and shape similar to that of the pristine material. A few new peaks with low intensity still appear in the fully discharged diffraction (the top line), which could be explained by the low Coulombic efficiency when using the operando cell with limited performance. The electrochemical data suggest that some Li remains in the structure, which is not observed when coin cells are prepared. Generally, based on the peak intensities and shapes after a full cycle, the same phase is obtained, and the volume expansion during the lithiation is minimal. Future measurements using a high-intensity light source can accurately determine the volume change as a function of the Li-ion insertion. Those measurements have been applied for other Wadsley−Roth material members that presented less than 10% volume expansion, such as $W_3Nb_{14}O_{44}$ with a total volume change of about 5.9%, $LiScMo_3O_8$ with 3%,[43] and $TiNb_2O_7$ with 7.22%.[44]

$NaNb_7O_{18}$ is clearly a promising candidate for fast-charging electrodes based on the electrochemical data that show small capacity loss between 2, 5, and 10C during charging along with minimal structural changes after a full cycle. To learn about the charge storage mechanisms in the structure, we performed potentiometric entropy measurements, which determined the open-circuit voltage $U_{OCV}(x,T)$ and the entropic potential $\partial U_{OCV}(x,T)/\partial T$. Both $U_{OCV}(x,T)$ and $\partial U_{OCV}(x,T)/\partial T$ relate to fundamental thermodynamic quantities of the electrodes according to the Nernst equation and Gibbs energy law.[21] Figure 5 shows the open-circuit voltage $U_{OCV}(x,T)$ and the

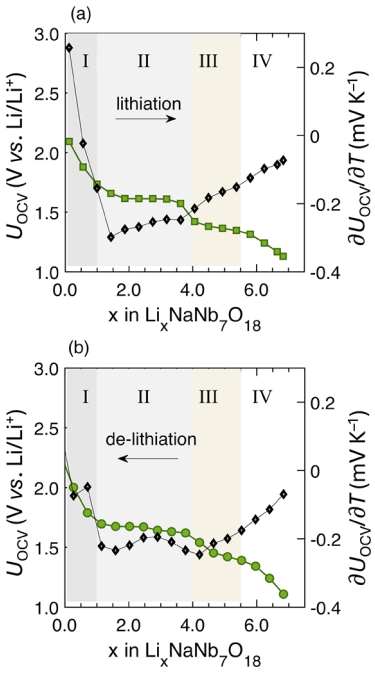

Figure 5. Potentiometric entropy measurements of $NaNb_7O_{18}$ vs Li. The open-circuit voltage $U_{OCV}(x)$ and the entropic potential $\partial U_{OCV}(x)/\partial T$ as functions of Li composition x are displayed during (a) lithiation and (b) delithiation cycling at a C/10 rate at 20 °C.

entropic potential $\partial U_{OCV}(x,T)/\partial T$ during (a) lithiation and (b) delithiation. We identified four different regions. First, in region I ($0 \leq x < 1.0$), both $U_{OCV}(x,T)$ and $\partial U_{OCV}(x,T)/\partial T$ decrease sharply with increasing x corresponding to Li insertion in a homogeneous solid solution.[21] In region II ($1.0 \leq x < 4.0$), $U_{OCV}(x,T)$ features a plateau indicating the first two-phase coexistence.[21] Interestingly, in particular, during delithiation, $\partial U_{OCV}(x,T)/\partial T$ shows a tilde-shaped fluctuation typically associated with intralayer ion ordering.[21] Therefore, we hypothesize that while the structure undergoes two-phase

https://doi.org/10.1021/acs.chemmater.4c02980
Chem. Mater. XXXX, XXX, XXX−XXX

reactions, intralayer ion ordering also occurs within either or both of the two phases. This feature could also play a role in the high rate performance, which is consistent with our previous studies on other Wadsley−Roth structure materials with ion ordering and generally demonstrating outstanding fast-charging capability.[21,28] Similarly, in region III ($4.0 \leq x < 5.5$), another plateau in $U_{OCV}(x,T)$ is observed, indicating the second two-phase coexistence.[21] In addition, $\partial U_{OCV}(x,T)/\partial T$ showed another tilde-shaped fluctuation, albeit not as visible as in region II, with the continued presence of intralayer ion ordering.[21] Finally, in region IV ($5.5 \leq x < 7.0$), $U_{OCV}(x,T)$ decreased monotonously, while $\partial U_{OCV}(x)/\partial T$ increased monotonously, which is also characteristic of Li insertion in a homogeneous solid solution.[21] Overall, all of the features above were repeatable between lithiation and delithiation as the material cycled reversibly. Furthermore, within regions II and III, the potentials where the two-phase reactions took place were consistent with those observed from operando XRD. It should be noted that, compared to the cases from previous studies,[21,28] the magnitude of the tilde-shaped fluctuation in $\partial U_{OCV}(x)/\partial T$ was relatively small. This reflects a minimal difference between the energies of various sublattice sites.[21] Thus, the migration barriers for Li insertion at different sublattice sites should be very low. Therefore, this would lead to the case of two-phase reactions with a low preference for site occupation.

The results obtained on $NaNb_7O_{18}$ encourage us to broaden our conclusion by looking at two kinetic parameters for five different Wadsley−Roth compounds. The ion diffusion coefficient (D) is a key parameter in the literature that quantifies ion transport in solids. The conventional way to find D is to apply Fick's second law. The concentration of ions can be challenging to measure in a closed system, such as a cell. GITT is often used to extract the apparent diffusion coefficient by measuring the voltage profile during a sequence of current pulses followed by rest periods.[19,45] The measured voltage can be converted to the concentration using the Nernst equation and plugged back into Fick's second law. This can be true as long as the voltage represents the changes in the ion concentration. As discussed in the previous section, the reaction occurs in a few ways. For a pure two-phase reaction, the voltage stays constant until the new phase is formed, and ion transport is not Fickian. Hence, the true diffusion coefficient cannot be extracted from GITT (or other impedance techniques) during a pure two-phase reaction. However, the two-phase reaction is only part of the Li insertion process, and we can use the other parts of the reaction to learn about the diffusion behavior. Figure 6a summarizes, in a box plot, the diffusion coefficients during Li-ion insertion for $NaNb_7O_{18}$ and four other Wadsley−Roth compounds made by solid-state synthesis (see the SI). Those anodes were cycled using the GITT methods, where the current pulse was set to a C/20 rate, followed by 3 h of relaxation between each current pulse. The open-circuit voltage was recorded and used later for further analysis of the overpotential. The box represents less than $\pm 1\sigma$, and the open circles are the outliers that differ significantly from the rest of the data set ($>\pm 3\sigma$).

The data collected by GITT can be used to calculate the overpotential of Li insertion, representing the energy of adding and/or removing ions to and/or from the structure. The overpotential is calculated from the voltage gap between the end of the current pulse step and the open-voltage circuit after

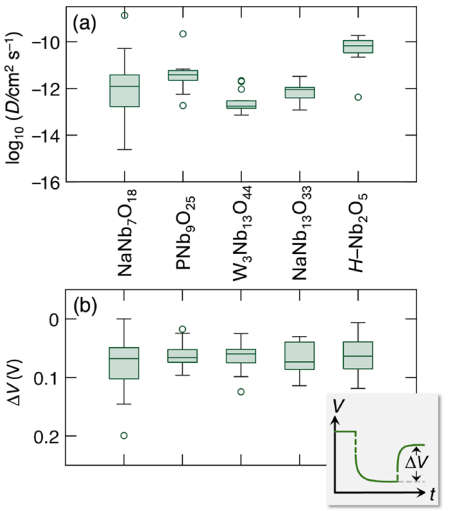

Figure 6. (a) Diffusion coefficient $\log_{10}(D)$ and (b) overpotential ΔV during the charging process for different shear-structured Nb-oxide anode materials. The box represents less than $\pm 1\sigma$ and the open circles are the outliers ($>\pm 3\sigma$). Individual GITT measurements can be found in the SI.

the system relaxes to an equilibrium (Figure 6b). The larger this value, the higher the energy required for Li insertion into a compound. Similar to the diffusion coefficient, there is only a small variation among the compounds. The materials are ordered from the least sloped $I-V$ curve to the most sloped curve. A sloped curve represents a solid solution process, and flat regions (plateaux) correspond to a two-phase reaction. The measured diffusion values are between 10^{-14} and 10^{-10} $\mathrm{cm}^2\ \mathrm{s}^{-1}$ for all five compounds with no clear trend of whether the GITT is sloped or shows flat regions.

In conclusion, $NaNb_7O_{18}$ has been established as a member of the Wadsley−Roth family of oxide compounds that is extremely effective as a fast-charging anode for Li-ion batteries, with exceptional performance, including capacity retention even after 1000 cycles. Given the relatively elevated anode voltage, we anticipate that when this material is coupled with a high-voltage cathode, acceptable full-cell energy densities can be accessed. This compound is highly ordered, and Li insertion takes place mainly through two-phase reactions, which is somewhat surprising for a material displaying fast charging. Potentiometric entropy measurements confirm the two-phase reactions as the primary charge storage mechanism. They also provide evidence for intralayer ion ordering. In addition, we have shown that low migration barriers between different Li sites result in fast Li-ion insertion (within minutes rather than hours). The diffusion coefficients and overpotentials for other Wadsley−Roth members were found to be similar, showing that the type of reaction during intercalation does not appear to influence the kinetics. Low migration barriers are clearly the essential feature for fast insertion in electrode materials, and we believe this arises from rigid channels for Li-ion transport in the structure, consistent with the structural symmetry being conserved, with only minor changes in unit cell parameters.

■ ASSOCIATED CONTENT

Supporting Information

The Supporting Information is available free of charge at https://pubs.acs.org/doi/10.1021/acs.chemmater.4c02980.

https://doi.org/10.1021/acs.chemmater.4c02980
Chem. Mater. XXXX, XXX, XXX−XXX

Table describing the results of Rietveld refinement of synchrotron X-ray diffraction on $NaNb_7O_{18}$, bond valence analysis for Na-ion transport compared with Li-ion transport in $NaNb_7O_{18}$, complete operando X-ray diffraction on $NaNb_7O_{18}$ as a function of Li insertion, GITT plots for Li insertion for all five compounds (along with their preparation) that are discussed in Figure 6 (PDF)

AUTHOR INFORMATION

Corresponding Author

Ram Seshadri − *Materials Department and Materials Research Laboratory, University of California, Santa Barbara, California 93106, United States;* orcid.org/0000-0001-5858-4027; Email: seshadri@mrl.ucsb.edu

Authors

Arava Zohar − *Materials Department and Materials Research Laboratory, University of California, Santa Barbara, California 93106, United States;* orcid.org/0000-0002-8292-5968

Tianyu Li − *Materials Department and Materials Research Laboratory, University of California, Santa Barbara, California 93106, United States;* orcid.org/0000-0003-0142-7252

Yucheng Zhou − *Mechanical and Aerospace Engineering Department, Henry Samueli School of Engineering and Applied Science University of California, Los Angeles, California 90095, United States*

Kira E. Wyckoff − *Materials Department and Materials Research Laboratory, University of California, Santa Barbara, California 93106, United States;* orcid.org/0000-0003-4353-9447

Alexander Justice Bologna − *Department of Chemistry and Biochemistry, University of California, Santa Barbara, California 93106, United States;* orcid.org/0000-0001-8149-6965

Ashlea Patterson − *Materials Department and Materials Research Laboratory, University of California, Santa Barbara, California 93106, United States*

Laurent Pilon − *Mechanical and Aerospace Engineering Department, Henry Samueli School of Engineering and Applied Science University of California, Los Angeles, California 90095, United States*

Complete contact information is available at: https://pubs.acs.org/10.1021/acs.chemmater.4c02980

Notes

The authors declare no competing financial interest.

ACKNOWLEDGMENTS

This work was supported as part of the Center for Synthetic Control Across Length Scales for Advancing Rechargeables (SCALAR), an Energy Frontier Research Center funded by the U.S. Department of Energy, Office of Science, Basic Energy Sciences under Award DE-SC0019381. A.Z. gratefully acknowledges the Elings Postdoctoral Fellowship Program for support. The research made use of shared facilities of the UC Santa Barbara MRSEC (NSF DMR 2308708), a member of the NSF-supported Materials Research Facilities Network (www.mrfn.org). Use of the Stanford Synchrotron Radiation Lightsource, SLAC National Accelerator Laboratory, is supported by the U.S. Department of Energy, Office of Science, Office of Basic Energy Sciences under contract no. DE-AC02-76SF00515.

REFERENCES

(1) Kang, K.; Meng, Y. S.; Bréger, J.; Grey, C. P.; Ceder, G. Electrodes with High Power and High Capacity for Rechargeable Lithium Batteries. *Science* **2006**, *311*, 977−980.

(2) Roberts, M. R.; Madsen, A.; Nicklin, C.; Rawle, J.; Palmer, M. G.; Owen, J. R.; Hector, A. L. Direct Observation of Active Material Concentration Gradients and Crystallinity Breakdown in $LiFePO_4$ Electrodes During Charge/Discharge Cycling of Lithium Batteries. *J. Phys. Chem. C* **2014**, *118*, 6548−6557.

(3) Xu, C.; Märker, K.; Lee, J.; Mahadevegowda, A.; Reeves, P. J.; Day, S. J.; Groh, M. F.; Emge, S. P.; Ducati, C.; Mehdi, B. L.; Tang, C. C.; Grey, C. P. Bulk Fatigue Induced by Surface Reconstruction in Layered Ni-Rich Cathodes for Li-Ion Batteries. *Nat. Mater.* **2021**, *20*, 84−92.

(4) Simon, B.; Flandrois, S.; Guerin, K.; Fevrier-Bouvier, A.; Teulat, I.; Biensan, P. On the Choice of Graphite for Lithium Ion Batteries. *J. Power Sources* **1999**, *81*, 312−316.

(5) An, S. J.; Li, J.; Daniel, C.; Mohanty, D.; Nagpure, S.; Wood, D. L., III The State of Understanding of the Lithium-Ion-Battery Graphite Solid Electrolyte Interphase (SEI) and its Relationship to Formation Cycling. *Carbon* **2016**, *105*, 52−76.

(6) Verma, P.; Maire, P.; Novák, P. A Review of the Features and Analyses of the Solid Electrolyte Interphase in Li-Ion Batteries. *Electrochim. Acta* **2010**, *55*, 6332−6341.

(7) Wang, Y.; Guo, X.; Greenbaum, S.; Liu, J.; Amine, K. Solid Electrolyte Interphase Formation on Lithium-Ion Electrodes: A ^{7}Li Nuclear Magnetic Resonance Study. *Electrochem. Solid State Lett.* **2001**, *4*, A68.

(8) Griffith, K. J.; Harada, Y.; Egusa, S.; Ribas, R. M.; Monteiro, R. S.; Von Dreele, R. B.; Cheetham, A. K.; Cava, R. J.; Grey, C. P.; Goodenough, J. B. Titanium Niobium Oxide: From Discovery to Application in Fast-Charging Lithium-Ion Batteries. *Chem. Mater.* **2021**, *33*, 4−18.

(9) Wang, M.; Yao, Z.; Li, Q.; Hu, Y.; Yin, X.; Chen, A.; Lu, X.; Zhang, J.; Zhao, Y. Fast and Extensive Intercalation Chemistry in Wadsley-Roth Phase Based High-Capacity Electrodes. *J. Energy Chem.* **2022**, *69*, 601−611.

(10) Xie, F.; Xu, J.; Liao, Q.; Zhang, Q.; Liu, B.; Shao, L.; Cai, J.; Shi, X.; Sun, Z.; Wong, C.-P. Progress in Niobium-Based Oxides as Anode for Fast-Charging Li-Ion Batteries. *Energy Rev.* **2023**, *2*, No. 100027.

(11) Voskanyan, A. A.; Navrotsky, A. Shear Pleasure: The Structure, Formation, and Thermodynamics of Crystallographic Shear Phases. *Annu. Rev. Mater. Res.* **2021**, *51*, 521−540.

(12) Preefer, M. B.; Saber, M.; Wei, Q.; Bashian, N. H.; Bocarsly, J. D.; Zhang, W.; Lee, G.; Milam-Guerrero, J.; Howard, E. S.; Vincent, R. C.; et al. Multielectron Redox and Insulator-to-Metal Transition upon Lithium Insertion in the Fast-Charging, Wadsley-Roth Phase PNb_9O_{25}. *Chem. Mater.* **2020**, *32*, 4553−4563.

(13) Radin, M. D.; Van der Ven, A. Simulating Charge, Spin, and Orbital Ordering: Application to Jahn−Teller Distortions in Layered Transition-Metal oxides. *Chem. Mater.* **2018**, *30*, 607−618.

(14) Bhattacharya, J.; Van der Ven, A. Phase Stability and Nondilute Li Diffusion in Spinel $Li_{1+x}Ti_2O_4$. *Phys. Rev. B* **2010**, *81*, No. 104304.

(15) Belak, A. A.; Wang, Y.; Van der Ven, A. Kinetics of Anatase Electrodes: the Role of Ordering, Anisotropy, and Shape Memory Effects. *Chem. Mater.* **2012**, *24*, 2894−2898.

(16) Griffith, K. J.; Wiaderek, K. M.; Cibin, G.; Marbella, L. E.; Grey, C. P. Niobium Tungsten Oxides for High-Rate Lithium-Ion Energy Storage. *Nature* **2018**, *559*, 556−563.

(17) Yang, Y.; Zhao, J. Wadsley−Roth Crystallographic Shear Structure Niobium-Based oxides: Promising Anode Materials for High-Safety Lithium-Ion Batteries. *Adv. Sci.* **2021**, *8*, No. 2004855.

(18) Patterson, A. R.; Elizalde-Segovia, R.; Wyckoff, K. E.; Zohar, A.; Ding, P. P.; Turner, W. M.; Poeppelmeier, K. R.; Narayan, S. R.;

Clément, R. J.; Seshadri, R.; Griffith, K. J. Rapid and Reversible Lithium Insertion in the Wadsley−Roth-Derived Phase $NaNb_{13}O_{33}$. *Chem. Mater.* **2023**, *35*, 6364−6373.
(19) Van der Ven, A.; Bhattacharya, J.; Belak, A. A. Understanding Li Diffusion in Li-Intercalation Compounds. *Acc. Chem. Res.* **2013**, *46*, 1216−1225.
(20) Koçer, C. P.; Griffith, K. J.; Grey, C. P.; Morris, A. J. Cation Disorder and Lithium Insertion Mechanism of Wadsley-Roth Crystallographic Shear Phases from First Principles. *J. Am. Chem. Soc.* **2019**, *141*, 15121−15134.
(21) Baek, S. W.; Saber, M.; Van der Ven, A.; Pilon, L. Thermodynamic Analysis and Interpretative Guide to Entropic Potential Measurements of Lithium-Ion Battery Electrodes. *J. Phys. Chem. C* **2022**, *126*, 6096−6110.
(22) Clément, R.; Lun, Z.; Ceder, G. Cation-Disordered Rocksalt Transition Metal Oxides and Oxyfluorides for High Energy Lithium-Ion Cathodes. *Energy & Env. Sci.* **2020**, *13*, 345−373.
(23) Marinder, B.-O.; Sundberg, M. The Structure of $NaNb_7O_{18}$ as Deduced from HREM Images and X-ray Powder Diffraction Data. *Acta Crystallogr. B* **1984**, *40*, 82−86.
(24) Deiss, E. Spurious Chemical Diffusion Coefficients of Li^+ in Electrode Materials Evaluated with GITT. *Electrochim. Acta* **2005**, *50*, 2927−2932.
(25) Kim, J.; Park, S.; Hwang, S.; Yoon, W.-S. Principles and Applications of Galvanostatic Intermittent Titration Technique for Lithium-Ion Batteries. *J. Electrochem. Sci. Technol.* **2022**, *13*, 19−31.
(26) Coelho, A. A. TOPAS and TOPAS-Academic: An Optimization Program Integrating Computer Algebra and Crystallographic Objects Written in C++. *J. Appl. Crystallogr.* **2018**, *51*, 210−218.
(27) Momma, K.; Izumi, F. *VESTA 3* for Three-Dimensional Visualization of Crystal, Volumetric and Morphology Data. *J. Appl. Crystallogr.* **2011**, *44*, 1272−1276.
(28) Baek, S. W.; Wyckoff, K. E.; Butts, D. M.; Bienz, J.; Likitchatchawankun, A.; Preefer, M. B.; Frajnkovič, M.; Dunn, B. S.; Seshadri, R.; Pilon, L. Operando Calorimetry Informs the Origin of Rapid Rate Performance in Microwave-prepared $TiNb_2O_7$ Electrodes. *J. Power Sources* **2021**, *490*, No. 229537.
(29) Zhou, Y.; Luo, Y.; Patterson, A.; Baek, S. W.; Frajnkovič, M.; Seshadri, R.; Dunn, B. S.; Pilon, L. Microcalorimetry Electrothermal Impedance Spectroscopy (ETIS) Informs Entropy Evolution at Individual Electrodes of PNb_9O_{25} or $TiNb_2O_7$ Battery Cells. *Electrochim. Acta* **2023**, *468*, No. 143072.
(30) Shafer, M.; Roy, R. Phase Equilibria in the System Na_2O−Nb_2O_5. *J. Am. Ceram. Soc.* **1959**, *42*, 482−486.
(31) McCarroll, W. H.; Katz, L.; Ward, R. Some Ternary Oxides of Tetravalent Molybdenum. *J. Am. Chem. Soc.* **1957**, *79*, 5410−5414.
(32) Hardcastle, F. D.; Wachs, I. E. Determination of Niobium-Oxygen Bond Distances and Bond Orders by Raman Spectroscopy. *Solid State Ionics* **1991**, *45*, 201−213.
(33) Huang, B. X.; Wang, K.; Church, J. S.; Li, Y.-S. Characterization of Oxides on Niobium by Raman and Infrared Spectroscopy. *Electrochimica acta* **1999**, *44*, 2571−2577.
(34) Pittman, R. M.; Bell, A. T. Raman Studies of the Structure of Niobium Oxide/Titanium Oxide (Nb_2O_5.TiO_2). *J. Phys. Chem.* **1993**, *97*, 12178−12185.
(35) Han, J. T.; Huang, Y. H.; Goodenough, J. B. New Anode Framework for Rechargeable Lithium Batteries. *Chem. Mater.* **2011**, *23*, 2027−2029.
(36) Brown, I. D. Recent Developments in the Methods and Applications of the Bond Valence Model. *Chem. Rev.* **2009**, *109*, 6858−6919.
(37) Chen, H.; Wong, L. L.; Adams, S. SoftBV−A Software Tool for Screening the Materials Genome of Inorganic Fast Ion Conductors. *Acta Cryst. B. Struct. Sci. Cryst. Eng. Mater.* **2019**, *75*, 18−33.
(38) Wong, L. L.; Phuah, K. C.; Dai, R.; Chen, H.; Chew, W. S.; Adams, S. Bond Valence Pathway Analyzer—An Automatic Rapid Screening Tool for Fast Ion Conductors within softBV. *Chem. Mater.* **2021**, *33*, 625−641.
(39) Wyckoff, K. E.; Robertson, D. D.; Preefer, M. B.; Teicher, S. M.; Bienz, J.; Kautzsch, L.; Mates, T. E.; Cooley, J. A.; Tolbert, S. H.; Seshadri, R. High-Capacity Li^+ Storage through Multielectron Redox in the Fast-Charging Wadsley−Roth phase $(W_{0.2}V_{0.8})_3O_7$. *Chem. Mater.* **2020**, *32*, 9415−9424.
(40) Lou, S.; Cheng, X.; Gao, J.; Li, Q.; Wang, L.; Cao, Y.; Ma, Y.; Zuo, P.; Gao, Y.; Du, C.; Huo, H.; Yin, G. Pseudocapacitive Li^+ Intercalation in Porous $Ti_2Nbi_{10}O_{29}$ Nanospheres Enables Ultra-Fast Lithium Storage. *Energy Storage Mater.* **2018**, *11*, 57−66.
(41) Deng, Q.; Fu, Y.; Zhu, C.; Yu, Y. Niobium-Based Oxides Toward Advanced Electrochemical Energy Storage: Recent Advances and Challenges. *Small* **2019**, *15*, No. e1804884.
(42) Saber, M.; Preefer, M. B.; Kolli, S. K.; Zhang, W.; Laurita, G.; Dunn, B.; Seshadri, R.; Van der Ven, A. Role of Electronic Structure in Li Ordering and Chemical Strain in the Fast Charging Wadsley−Roth Phase PNb_9O_{25}. *Chem. Mater.* **2021**, *33*, 7755−7766.
(43) Wyckoff, K. E.; Kaufman, J. L.; Baek, S. W.; Dolle, C.; Zak, J. J.; Bienz, J.; Kautzsch, L.; Vincent, R. C.; Zohar, A.; See, K. A.; Eggeler, Y. M.; Pilon, L.; Van der Ven, A.; Seshadri, R. Metal−Metal Bonding as an Electrode Design Principle in the Low-Strain Cluster Compound $LiScMo_3O_8$. *J. Am. Chem. Soc.* **2022**, *144*, 5841−5854.
(44) Yan, L.; Shu, J.; Li, C.; Cheng, X.; Zhu, H.; Yu, H.; Zhang, C.; Zheng, Y.; Xie, Y.; Guo, Z. $W_3Nb_{14}O_{44}$ nanowires: ultrastable lithium storage anode materials for advanced rechargeable batteries. *Energy Storage Mater.* **2019**, *16*, 535−544.
(45) Dees, D. W.; Kawauchi, S.; Abraham, D. P.; Prakash, J. Analysis of the Galvanostatic Intermittent Titration Technique (GITT) as Applied to a Lithium-Ion Porous Electrode. *J. Power Sources* **2009**, *189*, 263−268.

https://doi.org/10.1021/acs.chemmater.4c02980
Chem. Mater. XXXX, XXX, XXX−XXX